JGR Space Physics

RESEARCH ARTICLE
10.1029/2019JA027469

On the Confinement of Ultrarelativistic Electron Remnant Belts to Low L Shells

V. A. Pinto[1,2], X.-J. Zhang[1,3], D. Mourenas[4], J. Bortnik[1], A. V. Artemyev[3], L. R. Lyons[1], and P. S. Moya[5]

[1]Department of Atmospheric and Oceanic Sciences, University of California, Los Angeles, CA, USA, [2]Now at Institute for the Study of Earth, Oceans, and Space, University of New Hampshire, Durham, NH, USA, [3]Department of Earth, Planetary, and Space Sciences, University of California, Los Angeles, CA, USA, [4]CEA, DAM, DIF, Arpajon, France, [5]Departamento de Física, Facultad de Ciencias, Universidad de Chile, Santiago, Chile

Key Points:
- Outward radial diffusion by ULF waves may be crucial for the confinement of multi-MeV remnant belts to low L shells
- ULF wave power and radial diffusion rates are correlated with remnant belts upper edge and last closed drift shell
- Contemporaneous EMIC and chorus waves could play a role during some events by quickly precipitating multi-MeV electrons into the atmosphere

Supporting Information:
- Supporting Information S1

Correspondence to:
V. Pinto,
victor.pinto@gmail.com

Citation:
Pinto, V. A., Zhang, X.-J., Mourenas, D., Bortnik, J., Artemyev, A. V., Lyons, L. R., & Moya, P. S. (2020). On the confinement of ultrarelativistic electron remnant belts to low L shells. *Journal of Geophysical Research: Space Physics*, *125*, e2019JA027469. https://doi.org/10.1029/2019JA027469

Received 28 SEP 2019
Accepted 21 FEB 2020
Accepted article online 25 FEB 2020

Abstract Ultrarelativistic electron remnant belts are frequently observed at low L shells between the inner belt and a re-forming outer belt following geomagnetic disturbances that led to a dropout of electron fluxes at higher radial distances from the Earth. Using wave, particle, and plasma measurements from the Van Allen Probes and Pc3-Pc5 ultra low frequency (ULF) wave data from ground magnetometers from September 2012 to November 2017, we find significant correlations between the upper edge of the remnant belts and the minimum plasmapause and last closed drift shell locations. The maximum 2-hr-averaged radial diffusion rate based on ULF wave power recorded during the dropouts is correlated with the upper edge of the remnant belts and last closed drift shell position. Frequently, ULF wave power is sufficiently strong down to the upper edge of the remnant belts to allow a fast outward radial diffusion of electrons up to the last closed drift shell and to account for the observed confinement of remnant belts to low L shells. The electron phase space density often exhibits the needed negative or oscillating outward gradients in the region of flux loss. Accordingly, fast outward radial diffusion by ULF waves turns out to be a crucial contributor to the depletion of the outer belt that leads to the formation of remnant belts of ultrarelativistic electrons, although we show that multi-MeV electron precipitation through combined scattering by contemporaneous electromagnetic ion cyclotron (EMIC) and lower-band chorus waves probably contributes in a limited number of cases.

Plain Language Summary The Earth's Van Allen radiation belts are a very dynamic region in the near-Earth magnetosphere where extremely energetic electrons can be trapped, transported, energized, and removed over periods of minutes to weeks. There are generally two belts filled with significant electron flux and a gap in between them. However, after certain geomagnetic disturbances, a three-belt configuration of electron flux appears following a partial removal of the outer belt, followed by a partial re-population, leaving a gap in between the remnant belt and new outer belt. In this work, we study possible mechanisms that determine the extent of the partial removal of the outer belt for a significant number of events that occurred between September 2012 and November 2017. We found that the main mechanism removing the outer belt is likely fast transport of particles to regions far from Earth, followed by loss of such electrons to the interplanetary medium, although sometimes precipitation of particles into the Earth's atmosphere can also contribute.

1. Introduction

Early observations from the Van Allen Probes (Mauk et al., 2013) revealed the existence of a special transient configuration of the Earth's radiation belts; a remnant belt of ultrarelativistic (multi-MeV) electron flux located at approximately $3.0 < L < 3.5$ formed in between the usual inner belt and a re-forming outer belt at larger radial distances from Earth (Baker et al., 2013) that lasted for a month in September 2012. Turner et al. (2013), through a statistical analysis using data from the Time History of Events and Macroscale Interactions during Substorms (THEMIS) satellites, suggested that such a configuration was infrequent but not unique and that it likely corresponded to a depletion of the outer belt at high L shells, leaving behind a remnant belt clearly separated from the naturally re-forming outermost radiation belt. The physical mechanisms potentially leading to the formation of a remnant belt have been investigated in many recent works (Mann

et al., 2016, 2018; Shprits et al., 2013, 2018; Thorne et al., 2013) that focused on the September 2012 event, but to date, the problem remains controversial and far from a definitive answer.

Turner et al. (2013) reported and analyzed 13 remnant belt occurrences by looking at phase space density (PSD) data from the THEMIS satellites, and Yuan and Zong (2013) reported and studied eight events using the SAMPEX data. Nevertheless, no statistical study focusing on the formation of the remnant belts has yet been performed. Remnant belts can exist for electrons between hundreds of keV and multi-MeV, and recently, a statistical survey of ultrarelativistic electron remnant belts (hereafter simply called "URRBs") observed by the Van Allen Probes between September 2012 and November 2017 by Pinto et al. (2018) found and characterized 30 such events and confirmed that remnant belt lifetimes increase with electron energy from days to months. Such increase in lifetime is being mainly determined by plasmaspheric hiss wave-induced scattering into the atmosphere (Lyons et al., 1972; Mourenas et al., 2017), although the additional presence of electromagnetic ion cyclotron (EMIC) waves can sometimes amplify loss for >2-MeV electrons (Pinto et al., 2019; Thorne et al., 2013; Turner et al., 2013).

In the present paper, we consider events first reported by Pinto et al. (2018). The electron data corresponds to spin-averaged omnidirectional flux measurements above 1.8 MeV from the Energetic Particle, Composition, and Thermal Plasma Suite (Spence et al., 2013) Relativistic Electron Proton Telescope (Baker et al., 2013) (ECT-REPT) on board the Van Allen Probes. Measurements from RBSP-A and RBSP-B were combined into a single grid of points binned in space ($\Delta L = 0.1$) and time ($\Delta t = 4.5$ hr) by averaging all available data between 1 September 2012 and 30 November 2017. From the data, 30 triple-belt events were found each with an associated ultrarelativistic remnant belt indicated in a clearly defined double peak in fluxes across the outer belt. To avoid issues with the background level of the instruments, a minimum flux of at least >25 cm^{-2} sr^{-1} s^{-1} was required for URRB selection (see also for more information Claudepierre et al., 2015; Moya et al., 2017). A close inspection of these 30 events shows that 18 of them correspond to a sudden dropout of 4-MeV electron flux (by at least a factor 3 in less than 10 hr) leading to a significant reduction (by at least 0.5 Earth radius) of the outward extent of the outer radiation belt of ultrarelativistic electrons at $L > 4$–4.5, meaning that the low L remnant belts were indeed significantly shaped by such events.

In the following sections, we focus on these 18 particular URRBs, where clear dropouts are seen over finite time intervals (listed in supporting information Table S1). We examine the relationships between remnant belt location, minimum last closed drift shell, minimum plasmapause position, and the magnitude of ultra low frequency (ULF) wave-driven radial diffusion at $L \sim 3.9$–4.6, to check whether a fast outward radial diffusion by intense ULF waves could account for the formation of these 18 remnant belts (Mann et al., 2016, 2018; Turner et al., 2013). The role of contemporaneous EMIC and chorus waves in biting off the initial outer part of the remnant belts (Li et al., 2007; Mourenas et al., 2016; Shprits et al., 2018; Zhang et al., 2017) is also explored during several events with weak ULF wave power.

2. Statistical Relationships Between Remnant Belt Location, Last Closed Drift Shell, Plasmapause, and ULF Wave Power

2.1. Correlations With Minimum Plasmapause and Last Closed Drift Shell

Pinto et al. (2018) have shown that a significant number of URRBs start to form just after the magnetopause location is at its closest approach to the Earth, corresponding to a low position L_{LCDS} of the last closed drift shell, and that remnant belts assume their final shape at the time when SYM-H (and/or D_{st}) reach their minimum values during the subsequent geomagnetic disturbance. Hereafter, we focus on the short period of time of ~5–8 hr between the times of minimum L_{LCDS} and D_{st}, during which an electron flux dropout is observed by the Van Allen Probes at the outer edge of the remnant belt, leading to its sudden confinement to significantly lower L. Note that we focus here on the ~5- to 8-hr period corresponding to the most important dropout.

We estimate the minimum plasmapause position L_{pp} based on the plasma density N_e inferred from Van Allen Probes upper-hybrid resonance (HFR) (Kurth et al., 2015) or spacecraft potential (EFW) measurements (Kletzing et al., 2013) during the considered dropout intervals, calculating the minimum L_{pp} via the formula $N_e(L_{pp}) = \max[30, 15(6.6/L_{pp})^4]$ cm^{-3} (Li et al., 2015). In general, this estimate of L_{pp} accurately separates the plasmasphere and trough regions (Agapitov et al., 2019). However, such density measurements must be performed during the dropout interval and outside the ~12–19 MLT sector frequently occupied

by high-density plasmaspheric plumes, to prevent an overestimation of the minimum L_{pp} (Agapitov et al., 2019; Goldstein et al., 2014). Therefore, we only use plasma density inferred from Van Allen Probes data in the 20–24 MLT and 0–13 MLT sectors. When no Van Allen Probes estimate of L_{pp} is available in this MLT range during the considered dropout interval, we use the minimum L_{pp} (averaged over eight consecutive hours in MLT to reduce discrepancies with other methods) provided by test-particle simulations from Goldstein et al. (2014) with a root-mean-square error of ∼0.4 Earth radius. Finally, when no other estimate is available, we use the minimum statistical $L_{pp}(D_{st}, \text{MLT})$ given in equation (3) from O'Brien and Moldwin (2003) on the basis of Combined Release and Radiation Effects Satellite (CRRES) statistics, with a root-mean-square error of ∼0.53 Earth radius (all L_{pp} estimates are given in Table S1). The $L_{pp}(D_{st}, \text{MLT})$ model has been chosen based on the correlation found by Mann et al. (2013) between a deeper penetration of ULF wave power in the inner magnetosphere and a more negative D_{st}. The onset of enhanced convection and the magnitude of ring current penetration that control the access of ULF wave power to low L shells (Degeling et al., 2018; Mann et al., 2013; Rae et al., 2019) are probably better captured by D_{st} than by AE, which is more related to substorm occurrences.

It has been suggested that URRBs may result from a depletion of the outer belt at high L shells caused by loss across the magnetopause during magnetosphere compressions by strong solar wind impulses (often called magnetopause shadowing loss) and/or due to EMIC wave-induced electron precipitation into the atmosphere (Mann et al., 2016, 2018; Shprits et al., 2013, 2018; Turner et al., 2013; Yuan & Zong, 2013). Here, we use the LANL* neural network code (Yu et al., 2012) to calculate the last closed drift shell for 90° equatorial pitch angle electrons with the T96 (Tsyganenko, 1995) and TS05 (Tsyganenko, 2005) magnetic field models (the older T96 model sometimes gives results in better agreement with observations (e.g., see Ganushkina et al., 2013) and keep the minimum obtained value as an estimate of the minimum $L_{LCDS} \simeq L^*_{LCDS}(LANL*)$ beyond which particles are lost (see Table S2), with an uncertainty of ∼0.5–0.8 Earth radius that mainly depends on the accuracy of magnetic field models (Albert et al., 2018; Olifer et al., 2018). Although the adiabatically invariant L^* is slightly smaller than McIlwain L, the difference between them at $L < 5$–6 is generally much smaller than uncertainties related to magnetic field models, and it is hereafter neglected to first order.

A typical event of ultrarelativistic remnant belt formation that occurred on 20 January 2016 is displayed in Figure 1. The initial radiation belt of electrons at energies of $E = 3.4$, 4.2, and 5.2 MeV (panels a–c) extends up to $L \sim 5$ until roughly 10–11 UT, before a fast dropout leads over the next several hours to its confinement to $L \leq \max(L, \text{Remnant Belt}) \sim 3.5$, where the remnant belt's upper edge $\max(L, \text{Remnant Belt})$ is taken as the L shell where electron flux decreases to $\sim 1/e$ of its peak level at $E = 4.2$ MeV (blue dashed line). The last closed drift shell of trapped electrons (red solid line) reaches its lowest position $\min[L_{LCDS}] \sim 4.4$ near 9 UT on 20 January. The estimated plasmapause position L_{pp} (black dotted line) decreases to ≃2.75 at ∼13 UT on 20 January during the ∼9–14 UT dropout period, which appears to takes place between the time of minimum L_{LCDS} and the time ∼16 UT of minimum $D_{st} \simeq -93$ nT (panel d), during the main phase of the storm.

Figure 2 shows a significant correlation between the upper edge of the 18 considered URRBs and $\min[L_{pp}]$. The upper edge $\max(L, \text{Remnant Belt})$ of the URRBs is generally within ≈0.0–0.5 Earth radius of the minimum plasmapause L_{pp} and increases linearly with it, the best least squares fit indicating a significant correlation $R = 0.56$. The minimum L_{LCDS} is similarly well correlated ($R = 0.64$) with $\max(L, \text{Remnant Belt})$. In addition, Figure 2 indicates that both the upper edge of the URRBs and the minimum plasmapause position are often 1.0–1.5 Earth radii lower than the minimum L_{LCDS}. Ultrarelativistic electrons bouncing along geomagnetic field lines at $L > L_{LCDS}$ drift azimuthally around the Earth and encounter open field lines in less than 15 min, being then quickly lost into interplanetary space (Olifer et al., 2018; Schulz & Lanzerotti, 1974). However, Figure 2 shows that the drop of ultrarelativistic electron flux above $\sim \max(L, \text{Remnant Belt})$ that produces a remnant belt cannot be explained solely this way. There is in general a large radial distance of at least one Earth radius that separates this flux drop from the minimum L_{LCDS}. In contrast, the minimum plasmapause location L_{pp} follows much more closely the upper edge of URRBs in Figure 2. Therefore, the maximum outward extent of the remnant belts seems to be more determined by the minimum plasmapause position than by the minimum last closed drift shell.

The above results suggest that the physical mechanism responsible for the formation of URRBs could be related to magnetopause shadowing loss through the reduction of L_{LCDS} by a strong disturbance, but that an additional process is needed in between the last closed drift shell and the plasmapause to account for

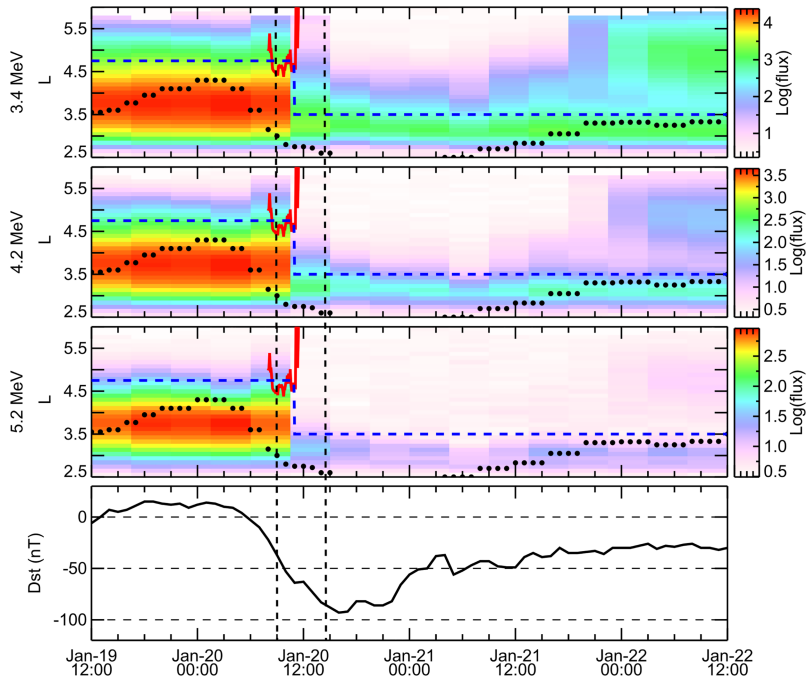

Figure 1. Formation of ultrarelativistic electron remnant belts (URRBs) observed on 20 January 2016 by the Van Allen Probes. (a–c) 3.4-, 4.2-, and 5.2-MeV electron flux from REPT as a function of time and L, plasmapause position L_{pp} from a test-particle simulation (Goldstein et al., 2014) (black dotted line), approximate last closed drift shell (red solid curve), and upper edge max(L, Remnant Belt) (blue dashed curve) of the peak flux of 4.2-MeV remnant belt electrons (that decreases down to max(L, Remnant Belt) $\simeq$ 3.5 after the dropout) are shown. (d) D_{st} index. Vertical dashed lines indicate the dropout period between ~9 UT (the approximate time of minimum $L_{LCDS} \simeq 4.4$) and 14 UT.

additional electron loss there. This additional electron loss may be caused by a fast outward radial diffusion by ULF waves (Mann et al., 2016, 2018; Ozeke et al., 2014; Schulz & Lanzerotti, 1974; Turner et al., 2013) or by precipitation into the atmosphere through combined scattering by contemporaneous EMIC waves in high-density plasmaspheric drainage plumes in the dusk sector and chorus waves just above the plasmapause in the dawn sector (Kersten et al., 2014; Li et al., 2007; Mourenas et al., 2016; Shprits et al., 2018; Turner et al., 2013; Zhang et al., 2017). Note that the D_{st} effect can also transport electrons outward during the decrease of D_{st}. However, it is an adiabatic effect such that electrons are generally transported back inward during storm recovery (Kim & Chan, 1997). In all the considered dropout events, no recovery of the ultrarelativistic electron flux is seen. Moreover, 60% (80%) of these events correspond to weak storms with $D_{st} \geq -40$ nT ($D_{st} \geq -70$ nT). During such weak storms, the radial displacement of electrons caused by the D_{st} effect should remain weak at low $L < 4.5$–5.0 where dropouts occur, requiring a strong outward radial diffusion combined with magnetopause shadowing or local losses to explain these dropouts.

In the following sections, we examine the possible roles played by electron outward radial diffusion by ULF waves, and by EMIC wave-induced precipitation, in the formation of the 18 considered URRBs in the 2012–2017 period.

2.2. Correlations With Radial Diffusion Rates of Remnant Belt and Last Closed Drift Shell

In the presence of a decreasing electron phase space density (PSD) toward higher L, where the closest approach of the last closed drift shell of trapped electrons at $L \simeq L_{LCDS}$ has just produced a deep minimum, ultrarelativistic electrons can be diffused radially outward by ULF waves and ultimately get lost on open field lines (Albert et al., 2018; Olifer et al., 2018; Ozeke et al., 2014; Schulz & Lanzerotti, 1974). The strength of the electron radial diffusion by ULF waves is usually largely determined by (and proportional to) the level of equatorial azimuthal electric field ULF wave power, which can be estimated from ground D-component magnetometer measurements under the assumption of a 90° polarization rotation through the ionosphere (Ozeke et al., 2014). Outward radial diffusion can be very fast during disturbed periods and lead to significant variations in electron fluxes over timescales of only a few hours (Mann & Ozeke, 2016; Mann et al., 2016; Murphy et al., 2015).

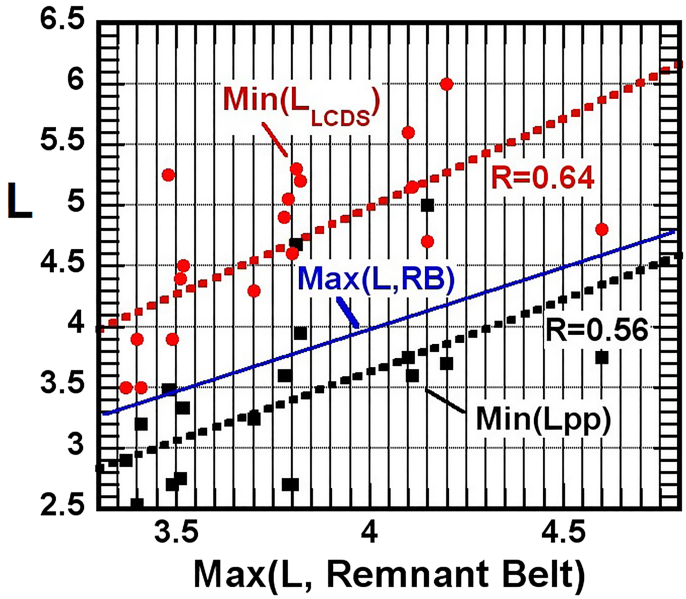

Figure 2. Minimum plasmapause position min[L_{pp}] (black squares) and minimum position of the last closed drift shell min[L_{LCDS}] (red circles) during the time interval of remnant belt formation, as a function of the upper edge max(L, Remnant Belt) (blue line) of the peak flux of remnant belt 4.2-MeV electrons, for the 18 URRBs suddenly confined to lower L shells observed by the Van Allen Probes in 2012–2017. Best least squares fits are shown by dotted lines of the same colors.

Recent works have revealed that intense ULF waves can reach low L shells down to the plasmapause location (Hartinger et al., 2010; Ren et al., 2017), especially at the times when the magnetosphere is most compressed (Murphy et al., 2015). Sometimes, ULF waves can travel through a plasmaspheric drainage plume of high-density plasma toward low L on the dayside (Degeling et al., 2018). Rae et al. (2019) have further shown that ULF wave power is often enhanced at low L during the main phase of strong geomagnetic storms, just before the minimum D_{st} is reached. These previous works therefore suggest that, although electrons may not have been immediately lost below $L \simeq L_{LCDS}$, they could still have been lost via a fast outward radial diffusion by intense ULF waves possibly present between the plasmapause and L_{LCDS} (Ozeke et al., 2019).

Assuming poloidal mode ULF waves and a general prevalence of electric field radial diffusion in ULF wave-particle interaction (e.g., Mann et al., 2013; Ozeke et al., 2014; Zong et al., 2009, 2017), the equatorial ULF wave electric field is first estimated based on ground magnetometer measurements of the D component of ULF waves (Ozeke et al., 2014; Wang et al., 2010), allowing to estimate the electric field radial diffusion coefficient D_{LL} at $L \sim 3.9$ and $L \sim 4.6$ in the same way as Ozeke et al. (2014). We consider the D-component ULF integrated magnetic wave power (in nT^2) measured in overlapping 2-hr moving windows in the 1.5-20 mHz range at $L \sim 3.9$ by the two stations at Prince George (PGE0) in British Columbia from the THEMIS GMAG network (Mende et al., 2008) and at Dombas (DOB) from the Tromso Geophysical University in Norway, as well as at $L \sim 4.6$ from stations at Meanook (MEA) from the University of Alberta and at Trapper Creek (TRAP) from the University of Alaska, and select the maximum 2-hr measured ULF wave power during the considered dropout periods (such values are provided in Table S2 for each event). At $L \sim 3.9$, considering the pair of stations PGEO-DOB allows to always use data from at least one dayside station, mitigating possible interferences in the ULF band from ionospheric currents in the ~21–03 MLT sector not corresponding to MHD waves in the equatorial magnetosphere (Murphy et al., 2015). Moreover, Ouyang et al. (2019) have shown that non-magnetospheric ULF waves present at $L \sim 4$ in the nightside ionosphere are in general much less intense than magnetospheric ULF waves during geomagnetic storms, and all the considered dropouts occurred during (weak to large) storms. In the following, we provide both D_{LL} inferred from ULF wave power at $L \sim 3.9$–4.6 measured at all MLT and a lower limit to the full D_{LL} inferred from ULF wave power measured only in the 05–19 MLT sector.

ULF wave power at low L is usually symmetric in MLT, but it can become more localized during strong solar wind disturbances (Hao et al., 2017; Li et al., 2017; Pahud et al., 2009). Individual magnetometer stations of the considered MEA-TRAP and PGEO-DOB pairs are respectively separated by 3 and 9 hr in MLT, providing

a limited MLT coverage. Accordingly, we assume that the measured ULF wave power from the MEA-TRAP and PGEO-DOB pairs of stations is present over ≈6 and 12 hr in MLT, respectively, and divide this measured ULF wave power by factors 6/24 and 12/24 to obtain rather conservative estimates of the MLT-averaged ULF wave power at $L \sim 3.9$ and 4.6 during the considered 2-hr periods. Such MLT-averaged ULF power values are then used to estimate $D_{LL}(L \sim 3.9)$ and $D_{LL}(L \sim 4.6)$ (Ozeke et al., 2014; Wang et al., 2010). Since D_{LL} varies like L^6 for fixed ULF wave power (Ozeke et al., 2014), we estimate the mean $\langle D_{LL} \rangle$ over a given region $3.4 \leq \max(L) < L_{LCDS}$ as

$$\langle D_{LL} \rangle \sim \frac{D_{LL}(L = 3.9)}{3.9^6} \frac{L_{LCDS}^7 - \max(L)^7}{7(L_{LCDS} - \max(L))}$$

for $L_{LCDS} \leq 4.2$. For $4.2 < L_{LCDS} \leq 5.0$, we use

$$\langle D_{LL} \rangle \sim \frac{D_{LL}(L = 3.9)}{3.9^6} \frac{(4.2^7 - \max(L)^7)}{7(L_{LCDS} - \max(L))} + \frac{D_{LL}(L = 4.6)}{4.6^6} \frac{L_{LCDS}^7 - 4.2^7}{7(L_{LCDS} - \max(L))}.$$

For events with $L_{LCDS} > 5.0$, we assume that ULF wave power at $L > 5$ is roughly given by the statistical empirical model $D_{LL,Oz}(\mathrm{Kp}, L)$ given in equation (23) from Ozeke et al. (2014), and we calculate

$$\langle D_{LL} \rangle \sim \frac{D_{LL}(L = 3.9)}{3.9^6} \frac{(4.2^7 - \max(L)^7)}{7(L_{LCDS} - \max(L))} + \frac{D_{LL}(L = 4.6)}{4.6^6} \frac{(5^7 - 4.2^7)}{7(L_{LCDS} - \max(L))} + \frac{L_{LCDS}^7 - 5^7}{5.7^6} \frac{D_{LL,Oz}(L = 5.7, \max(\mathrm{Kp}))}{7(L_{LCDS} - \max(L))}.$$

The corresponding estimates of the maximum 2-hr $\langle D_{LL} \rangle$ will be compared with statistical estimates $\langle D_{LL,Oz}(\mathrm{Kp}) \rangle$ based on the empirical model from Ozeke et al. (2014), considering the maximum Kp during each dropout period.

For each event, we check the presence of intense ULF waves in between the minimum last closed drift shell at $L \simeq L_{LCDS}$ and the upper remnant belt location. We inspect the period of remnant belt formation and select the 2-hr interval of the strongest ULF wave power located both (i) between the times when L_{LCDS} and D_{st} reach their minimum and (ii) during the ∼5- to 8-hr period when the most significant electron flux dropout occurs above the remnant belt in Van Allen Probes observations. This particular interval usually corresponds to the highest ULF wave power at low L shells (Murphy et al., 2015; Rae et al., 2019). Moreover, L_{LCDS} must already have reached its minimum to allow the development of a very fast electron flux dropout via outward radial diffusion toward higher L. This procedure is expected to yield a reasonable estimate of the maximal strength of outward radial diffusion at the corresponding L shells in the lead-up to remnant belt formation. For several events, we have also been able to confirm the occurrence of a drop of 4 MeV electron flux during the selected 2-hr periods by using higher-resolution (∼1–3 hr) near-equatorial electron flux measurements at $L = 4.1$–4.4 from combined X-ray dosimeters on board nine Global Positioning System (GPS) satellites designated as SVN53-61 (Morley et al., 2016).

Figures 3a and 3b reveal the presence of significant correlations $R \simeq 0.59$–0.69 between the maximum 2-hr-averaged $\langle D_{LL} \rangle$ at $L \simeq 3.9$ (estimated based on ULF wave power recorded on the ground) during the dropouts and both the upper edge $\max(L)$ of remnant belts and the minimum L_{LCDS}. Similar correlations are obtained when considering ULF wave power from all MLT sectors or only from the ∼5–19 MLT sector. Such correlations are consistent with previous works (Hartinger et al., 2010; Murphy et al., 2015; Ren et al., 2017) that demonstrated the propagation of ULF waves down to the plasmapause during episodes of strong magnetosphere compressions accompanied by plasmasphere erosion. In particular, Figure 3a shows that more ULF wave power reaches lower L shells when the dropout biting off the outer edge of the remnant belts simultaneously extends to lower L, since 63% to 100% of the events with remnant belt upper edge $\max(L) \leq 3.7$ correspond to $\langle D_{LL} \rangle(L = 3.9)$ larger than 1 per day, whereas for 90% of the events with $\max(L) \geq 3.8$, the radial diffusion rate $\langle D_{LL} \rangle(L = 3.9)$ remains smaller than 1 per day.

Figures 3c and 3d further show that during the 24 hr preceding the closest approach of the last closed drift shell (i.e., before an electron flux dropout creates the remnant belt), the maximum 2-hr ULF wave power at $L \simeq 3.9$ is usually ∼1.5 to 15 times smaller than the peak 2-hr ULF wave power found between the times of minimum L_{LCDS} and D_{st} during the dropout. Therefore, over the more than 24 hr preceding remnant belt formation, the peak ULF wave power is generally found between the times when L_{LCDS} and D_{st} successively

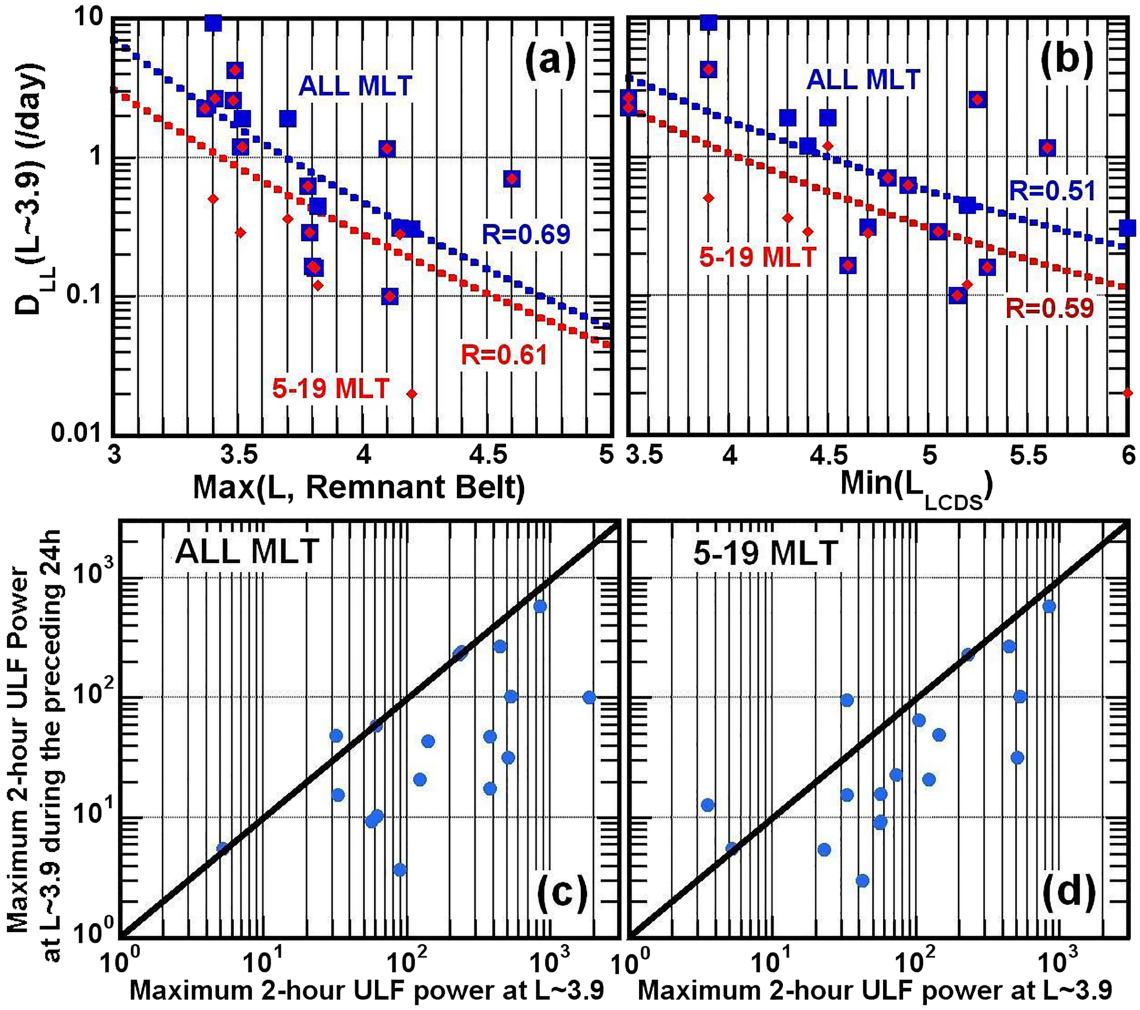

Figure 3. (a) Estimated maximum 2-hr-averaged radial diffusion rate $\langle D_{LL} \rangle$ at $L \simeq 3.9$ between the times of minimum L_{LCDS} and D_{st} during the observed electron flux dropouts above the remnant belts, as a function of the upper edge max(L) of remnant belts of 4.2-MeV electrons, for the 18 considered URRBs of 2012–2017. Values inferred from measured ULF wave power at all MLTs are shown by blue squares, and values obtained by considering only ULF wave power from stations in the ~5–19 MLT sector are shown by red diamonds. Best least squares fits to the data are shown by dotted lines of the same colors. (b) Same as (a), but as a function of the minimum L_{LCDS}. (c) Maximum 2-hr-averaged ULF wave power measured over 1.5–20 mHz at $L \simeq 3.9$ during a 2-hr period within the 24 hr preceding the minimum of L_{LCDS}, as a function of maximum 2-hr-averaged ULF wave power at $L \simeq 3.9$ between the times of minimum L_{LCDS} and D_{st} during the period of electron flux dropout above the 18 considered URRBs in 2012–2017. A solid black line indicates identical ULF wave powers. (d) Same as (c), but considering only ULF wave power from stations in the 05–19 MLT sector.

reach their minimum, in agreement with previous studies (Murphy et al., 2015; Rae et al., 2019). Although the maximum 2-hr ULF wave power recorded before the minimum L_{LCDS} still remains much stronger than the quiet time level of ~0.1 nT^2, averaging ULF wave power over the full preceding 24 hr yields much smaller levels ≈0.1–5 nT^2 in general. During the majority (~67% to 72%) of the events, the maximum 2-hr ULF wave power in the 24 hr preceding the minimum L_{LCDS} remains relatively moderate (<60 nT^2) at $L \simeq 3.9$. In such circumstances, intense ULF waves present at higher L shells before the considered $L \sim 4$ dropout could only drive electron outward radial diffusion nearby a much higher L_{LCDS}, leaving the $L \sim 4$ zone mostly unaffected.

Finally, it can be noticed in Figures 3c and 3d that for five URRBs, the maximum 2-hr ULF wave power recorded before the minimum L_{LCDS} was ~0.65 to 3 times the peak ULF wave power recorded just after the minimum L_{LCDS}. During such events, the electron flux dropout caused by outward radial diffusion may have started earlier, in the vicinity of a higher last closed drift shell, before ultimately reaching the lowest L. The remnant belt formed on 2–3 September 2012 is one of such five events, and Mann et al. (2016, 2018) have indeed shown that a simple model of radial diffusion based on measured ULF waves can reproduce

its formation over 1 day, provided that realistic energy-dependent and time-dependent electron fluxes are considered at the outer boundary $L \sim 5.6$.

The typical timescale of electron radial diffusion by ULF waves over a distance ΔL can be estimated as $\Delta t = (\Delta L)^2/[D_{LL}\Delta \ln(PSD)]$ (Ozeke et al., 2018; Schulz & Lanzerotti, 1974). Although the exact outward PSD gradient is unknown during the 2-hr periods of the dropouts, we hereafter assume a reasonable negative outward gradient of the electron PSD $\Delta \ln(PSD)/\Delta L \approx 1$ (to first order) between max(L) and L_{LCDS}, which yields a rough estimate $\Delta t \approx [L_{LCDS} - \max(L)]/D_{LL}$ of the timescale of electron outward radial diffusion from the upper edge max(L) of the remnant belts up to the minimum L_{LCDS}.

Significant correlations $R \simeq 0.53$–0.80 are found in Figure 4a between the maximum 2-hr $\langle D_{LL}\rangle$ estimated from ground magnetometer measurements over $\max(L) < L < L_{LCDS}$ during dropouts and the upper edge max(L) of the remnant belts. Although the maximum 2-hr $\langle D_{LL}\rangle$ varies strongly and can be ~1.5 to 100 times larger than statistical levels (Ozeke et al., 2014), it still increases approximately like L^6 on average, which theoretically corresponds to a constant ULF wave power independent of L (Ozeke et al., 2014). This means that the maximum 2-hr ULF wave power between max(L) and L_{LCDS} remains of the same order of magnitude during all the events, despite the important variations of max(L) and L_{LCDS} from one event to the other. No significant correlation is found between the statistical $\langle D_{LL,Oz}(\max(Kp))\rangle$ (Ozeke et al., 2014) and max(L), probably because the statistical radial diffusion rate depends strongly on the maximum Kp during the dropouts, which tends to increase for dropouts extending to lower L shells. As a result, the difference between maximum 2-hr and statistical diffusion rates decreases toward lower L in Figure 4a. Figure 4b shows that for 50% of the events, electrons starting at max(L) need a time $\Delta t \leq 2$ hr for reaching min(L_{LCDS}). Moreover, we recall that the displayed Δt values are based on conservative estimates of $\langle D_{LL}\rangle$, obtained by assuming that the measured ULF wave power is present over only 6(12) hr in MLT at $L \simeq 3.9(4.6)$. The actual $\langle D_{LL}\rangle$ could easily be twice larger than these conservative estimates. In such a case, electrons that apparently need a time $\Delta t \leq 4$ hr in Figure 4b to reach $L = L_{LCDS}$ could in fact reach it in less than 2 hr. This means that up to ~70% of the dropout events (with $\Delta t \leq 4$ hr, see dotted green line in Figure 4b) could actually be explained by a fast outward radial diffusion of electrons up to the last closed drift shell.

In addition, some of the dropouts may have occurred via outward radial diffusion over longer periods of ~4 to 5 hr, since ULF wave power does not suddenly decrease to zero just after the considered 2-hr periods. The initial electron PSD gradient may also have been sometimes steeper than assumed above, reducing Δt as compared with our simple estimates (Ozeke et al., 2018, 2019). Ozeke et al. (2018) have indeed shown that the early timescales of electron radial diffusion by 1 Earth radius over $L = 4$–5 can be less than ~3 hr when $Kp > 6$, later increasing as the gradient of electron PSD becomes less steep.

The above results show that ULF wave power is often sufficiently strong above the upper edge of the remnant belts to allow a fast outward radial diffusion of ultrarelativistic electrons up to the last closed drift shell, where they get lost. This suggests that fast outward diffusion associated to magnetopause shadowing loss could account for the formation of at least ~50–70% of the considered low-L remnant belts in 2012–2017. It also provides a plausible explanation for the good correlation found in Figure 2 between the minimum plasmapause and last closed drift shell positions and the maximum outward extension of the URRBs. Fast outward radial diffusion by powerful ULF waves toward the minimum last closed drift shell could simply drive a dropout of electron flux almost down to the plasmapause at $\min(L_{pp}) \approx \min(L_{LCDS}) - 1$ (Hartinger et al., 2010; Murphy et al., 2015; Ren et al., 2017), thereby creating a remnant belt confined to low L shells nearby and below the plasmapause.

2.3. Outward Gradient of Electron PSD During Dropouts

The loss of ultrarelativistic electrons through efficient ULF wave-driven outward radial diffusion actually requires that two conditions be satisfied: (1) sufficiently intense ULF waves and (2) the presence of a negative gradient of the electron PSD toward higher L (Schulz & Lanzerotti, 1974; Turner et al., 2013). The presence of a negative outward PSD gradient can be checked using Van Allen Probes data, making use of the PSD as a function of adiabatically invariant shells L^* calculated using the Tsyganenko-Sitnov TS05 magnetic field model (Tsyganenko, 2005) during these disturbances (Turner et al., 2012, 2013). Due to the fast decrease of the electron flux with energy above 2 MeV, however, the estimated PSD gradient is strongly dependent on the true magnitude of the magnetic field B through the first adiabatic invariant $\mu \simeq E(E+1)/B$ MeV/G, with B in Gauss and E electron energy in MeV. The inaccuracy of magnetic field models can result in significant errors of PSD, even at relatively low L (e.g., Green, 2004; Loridan et al., 2019; Ozeke et al., 2019). As we

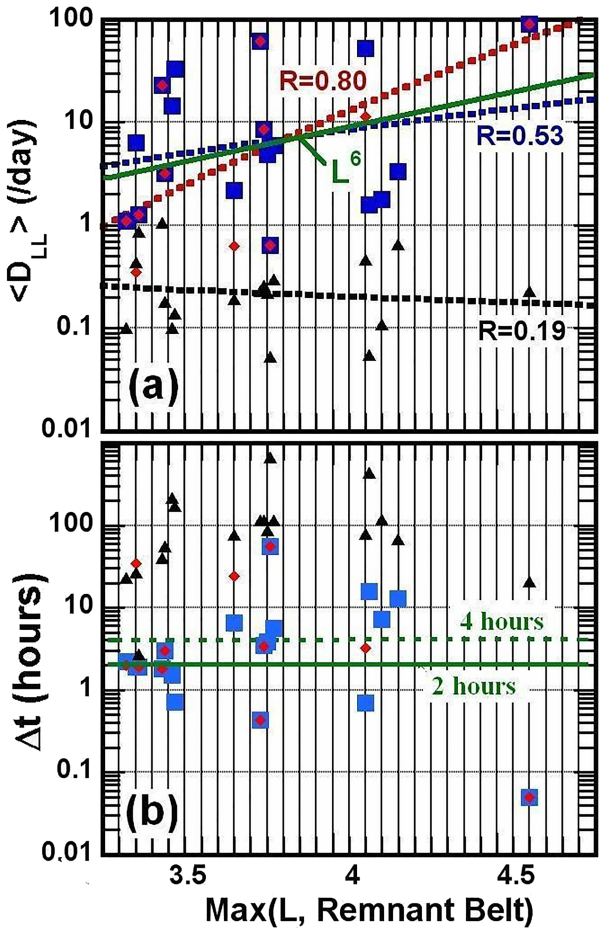

Figure 4. (a) Estimated maximum 2-hr radial diffusion rate $\langle D_{LL} \rangle$ over $\max(L) < L < L_{LCDS}$ between times of minimum L_{LCDS} and D_{st} during the observed dropouts above the 18 URRBs, as a function of the upper edge $\max(L)$ of remnant belts of 4-MeV electrons. Values inferred from measured ULF wave power at all MLTs are shown by blue squares, and values obtained with only ULF wave power from stations in the ~5–19 MLT sector are shown by red diamonds. Best least squares fits to the data are shown by dotted lines of same colors. $\langle D_{LL,Oz}\ \max(Kp) \rangle$ from a statistical model (Ozeke et al., 2014) is shown by black triangles. (b) Estimates of the timescale Δt of electrons outward radial diffusion from $\max(L)$ to L_{LCDS}, based on $\langle D_{LL} \rangle$ in (a) during the period of observed electron flux dropout, as a function of $\max(L)$. Values inferred from measured ULF wave power at all MLTs are shown by blue squares and values obtained with only ULF wave power in the ~5–19 MLT sector are shown by red diamonds. Best least squares fits to the data are shown by dotted lines of same colors. Values based on the statistical $\langle D_{LL,Oz}\ \max(Kp) \rangle$ (Ozeke et al., 2014) are shown by black triangles.

are using a model of the magnetic field, the estimated PSD(L^*) gradient must be considered with caution, especially during periods with electron flux oscillations. Accordingly, we hereafter focus on the 13 events during which no significant oscillation of 4 MeV electron flux is seen at $L \sim 4.0$–4.5 just after the dropout in Van Allen Probes data (see Table S1). During such events, the estimated radial PSD gradient is expected to be more reliable.

Let us consider the PSD at low second adiabatic invariant $K = 0.04\ G^{1/2}R_E$ (i.e., for large equatorial pitch angles) as a function of L^*, during two successive orbits of the Van Allen Probes separated by ~5 hr and delimiting the flux drop interval. For half of the considered events, we find a peak of PSD at the same location as the peak of 4 MeV electron flux of the URRB, but for the remaining events, only an inflection of the positive slope of the PSD is found. During the considered events, which generally correspond to weak storms with $D_{st} > -50$ nT, the remnant belt therefore shows up most frequently in electron fluxes. Between the upper edge $L^* \sim \max(L)$ of the URRB of 4 MeV electron flux and $L^* \sim \min(L_{LCDS})$, the PSD of $\mu \simeq 2{,}500$ MeV/G and $\mu \simeq 4{,}000$ MeV/G electrons exhibits a negative outward gradient (a steady decrease by a factor ≥ 2) during 7 to 8 of the 13 events during at least one of the two consecutive spacecraft orbits. For $\mu \simeq 4{,}000$ MeV/G, all the

events exhibit either a negative outward PSD gradient or some quasi-plateau with oscillations of less than a factor 2, with a PSD drop by a factor ~0.7 to 0.02 over $3.6 < L^* < 5$, and a minimum L^* of the PSD peak or quasi-plateau that remains less than 0.5 Earth radius above the upper edge of the URRB for most events (see Table S1). Consequently, at least 60% of these dropouts could be readily explained by the sole effect of outward radial diffusion by intense ULF waves toward a minimum of PSD at higher L shells produced earlier by magnetopause shadowing, following a sudden compression of the magnetosphere by the solar wind.

Van Allen Probes observations of an oscillating quasi-plateau of PSD instead of a negative outward PSD gradient may not seem very favorable for a fast electron loss via outward radial diffusion by ULF waves. However, Mann and Ozeke (2016) have demonstrated that the PSD could be very different in between two consecutive passages of the Van Allen Probes, which are separated by 4–5 hr. During this finite time interval, a drop of PSD may occur in less than 2 hr via strong outward radial diffusion by ULF waves at $L^* > 4$, after a strong and quick loss at $L \geq L_{\mathrm{LCDS}}$ (Olifer et al., 2018) that initially creates a steep negative outward PSD gradient at high L, and this negative PSD gradient may sometimes propagate afterwards to lower L^* through the effect of intense ULF waves (Mann & Ozeke, 2016; Mann et al., 2016, 2018). Various observations and simulations supporting the assumption of a formation by radial diffusion of a negative outward PSD gradient below the minimum L^*_{LCDS} are provided and discussed in a recent review by Turner and Ukhorskiy (2020). A simulation showing this effect is provided in Figure S1 from Mann et al. (2018). In addition, a negative outward PSD gradient below the minimum L^*_{LCDS} is often seen in observations just after L_{LCDS} has reached its minimum during storms (Olifer, 2019). The very steep negative outward gradient found in 3 MeV electron flux measured by GPS satellites below the lowest L^*_{LCDS} is also suggestive of the presence of a negative outward PSD gradient there (Olifer et al., 2018). Next, a strong peak of ~1-2 MeV electron PSD may be produced at $L^* > 5$ in less than 1–2 hr by ULF wave-driven inward radial diffusion (Mann & Ozeke, 2016) or by a fast local acceleration of 150-300 keV electrons by whistler-mode chorus waves (Agapitov et al., 2019; Kubota & Omura, 2018; Mourenas et al., 2018), finally creating a quasi-plateau of PSD (possibly even a positive outward gradient) at $\mu \sim$ 3,000–4,000 MeV/G. ULF wave-particle drift resonance can also play a role in the quick acceleration of ultrarelativistic electrons (Degeling et al., 2018; Hao et al., 2019). In principle, this whole scenario could easily take place in less than 3–4 hr and could generally go unnoticed in Van Allen Probes observations, due to the too long time interval (4–5 hr) separating successive spacecraft passages. Significant oscillations are frequently seen in the quasi-plateau of PSD and likely correspond to a dynamic PSD evolution consistent with this scenario. Therefore, the present Van Allen Probes observations of a quasi-plateau of PSD during 40% of the considered events do not rule out a dominant effect of ULF wave-driven outward radial diffusion even for such dropouts.

Let us now examine in detail a typical event that took place between 4 UT and 6 UT on 11 October 2017. This event corresponds to a weak magnetic storm with min(SYM-H) > −40 nT. Figures 5a and 5b show the presence of a negative outward PSD gradient at $L^* > 4$ near 1:10 UT and near 6:00 UT, inferred from Van Allen Probes measurements at $\mu =$ 2,500–6,000 MeV/G and $K = 0.04$ G$^{1/2}R_E$ (i.e., for $E \sim$ 3–5 MeV at $L^* \simeq 4$). There is a peak of PSD near $L^* \simeq$ 3.8–4.0 at the same location as the peak of 4 MeV electron flux of the URRB. Figure 5c displays the ratio of these two PSDs and shows a PSD drop down to 20% of its initial level between 1:10 UT and 6:00 UT over this $\mu =$ 2,500-6,000 MeV/G range, just after a minimum of $L_{\mathrm{LCDS}} \simeq 6.7$ is reached at around 4:30 UT (Figure 5f). Nearly simultaneously, a strong injection of electrons develops from the $L^* > 5$ region at $\mu <$ 300 MeV/G ($E < 0.5$ MeV), where the PSD gradient is positive as in previous statistics (Turner et al., 2012). The presence of electron inward radial diffusion, fast injections, or local chorus-driven energization during this limited time interval probably explains the much weaker dropouts at energies below ~1.5 MeV and low K, because radial diffusion and chorus-driven energization are often stronger at equatorial pitch angles $\alpha_{eq} > 50°$ (i.e., for $K < 0.1$ G$^{1/2}R_E$) and they develop only progressively from low to high energies (Li et al., 2014; Schulz, 1991).

Although Figure 5f shows that the minimum L_{LCDS} remains far above the upper edge of the URRB located at $L^* \simeq 4.2$, the dropout of 4 MeV electrons ultimately extends down to $L^* \simeq 4$ in Figure 5c. Additional measurements from GPS satellites (Morley et al., 2016) at $L =$ 4.1–4.4 displayed in Figure 5d reveal that this drop of 4 MeV electron flux mainly occurred between 4:40 UT and 6 UT, precisely during the first 2-hr period of elevated Pc4-Pc5 ULF wave power >60 nT^2 found in Figure 5e and selected for this event. Therefore, this dropout is fully consistent with a scenario of ultrarelativistic electron loss via outward radial diffusion by intense ULF waves toward the region of smaller PSD located at higher L^* near the minimum L_{LCDS}.

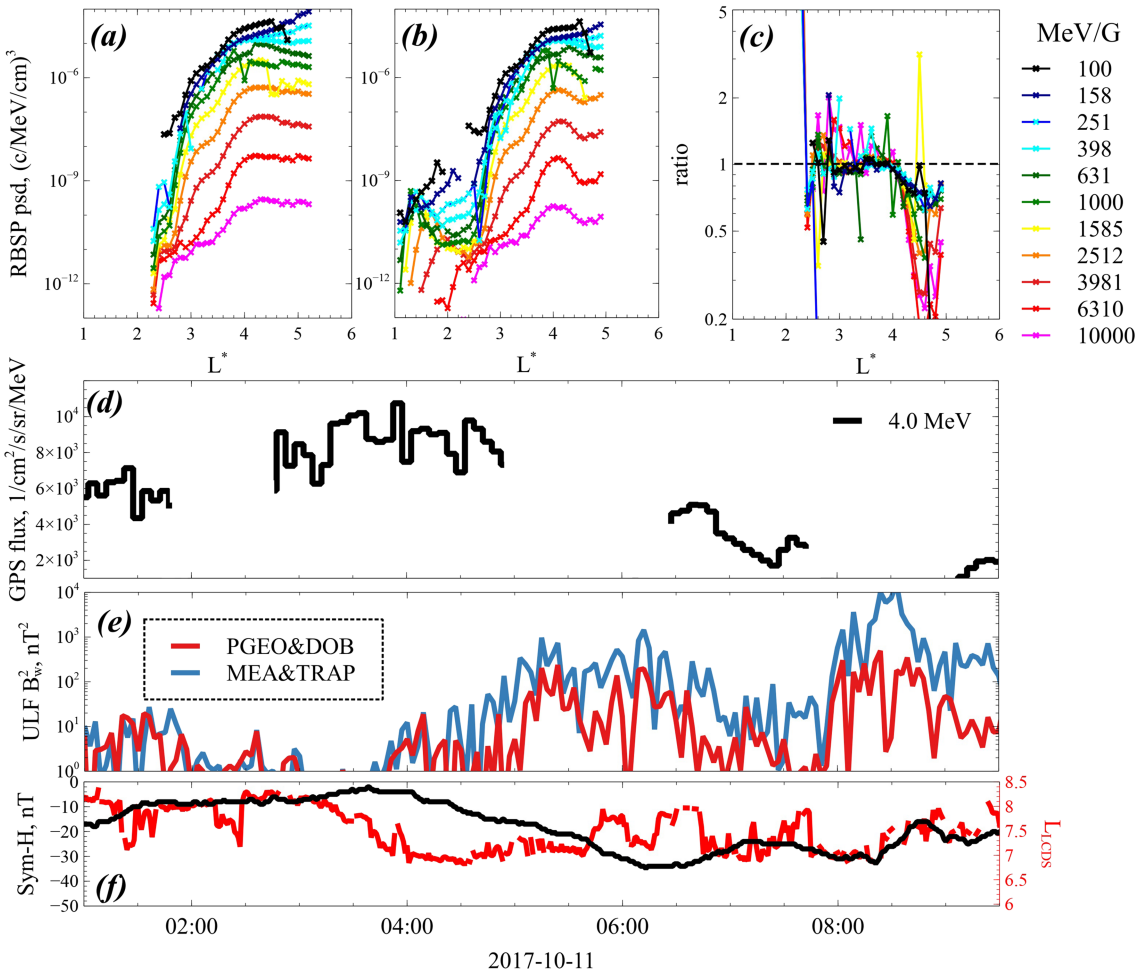

Figure 5. (a, b) Electron PSD radial profiles at 1:10 UT and 6:00 UT derived from REPT and MagEIS measurements on board the Van Allen Probes during two consecutive orbits preceding and following a dropout event on 11 October 2017 with fixed $K = 0.04$ G$^{1/2}R_E$. (c) Final to initial PSD ratio corresponding to (a) and (b). (d) 4 MeV electron flux measured by GPS satellites at $L \simeq 4.2$ during the same period. (e) ULF wave power (in nT^2) obtained from ground magnetometer stations. (f) Estimated L_{LCDS} and measured SYM-H over the same period.

3. Possible Role of EMIC and Chorus Waves in Multi-MeV Electron Flux Dropouts at $L \sim 4$–5

EMIC waves in the hydrogen band with an upper frequency cutoff around ~0.45 times the proton gyrofrequency, occurring in regions of elevated electron plasma frequency to gyrofrequency ratio $F_{pe}/F_{ce} \geq 15$ inside plasmaspheric drainage plumes at ~11–20 MLT, are generally the most efficient, in combination with contemporaneous chorus wave-driven pitch angle scattering above the dawnside plasmapause, for quickly precipitating whole populations (up to large equatorial pitch angles) of ~2-5 MeV electrons (Mourenas et al., 2016; Zhang et al., 2017). However, statistics of EMIC waves from the Van Allen Probes presented in Figure 2b from Zhang et al. (2016) for -650 nT$< AL *< -250$ nT ($AL*$ being the minimum AL in the preceding 3 hr), show a MLT-averaged occurrence rate of H-band EMIC waves of ~0.5% over $3.5 < L < 4.5$. Occurrences are roughly twice larger when $AL *< -650$ nT, but since such very active periods are much more rare than -650 nT$< AL *< -250$ nT periods, an average occurrence rate of ~0.5% over $3.5 < L < 4.5$ is a good estimate during $AL *< -250$ nT periods. This corresponds to time- and MLT-averaged EMIC wave intensity ≈0.0019 nT^2.

There were on average ~4 hr, and always less than 6 hr, of $AL < -250$ nT during the period of formation of the considered 18 URRBs in 2012–2017. Even in combination with contemporaneous intense lower-band chorus waves just above the plasmapause on the dawnside, H-band EMIC waves of such low time-averaged amplitudes are unlikely to drive a significant precipitation of ≃4.2-5.2 MeV electrons at $L \simeq 4$ over less

than 6 hr via quasi-linear pitch angle scattering (Mourenas et al., 2016), as would be needed to explain the formation of these URRBs. Of course, periods of unusually high time- and MLT-averaged EMIC wave intensity may still lead to dropouts of multi-MeV electrons at $L \simeq 4$ even when the magnetopause remains too far (Boynton et al., 2017; Xiang et al., 2018), allowing to form a remnant belt at lower L shells (Shprits et al., 2013, 2018)—but such strong EMIC wave events probably cannot explain alone the majority of the considered URRBs. Moreover, the time resolution of satellite observations (∼5–6 hr for the Van Allen Probes) is generally not sufficient to unambiguously distinguish electron flux dropouts caused by EMIC and chorus waves from dropouts produced by a fast outward radial diffusion by ULF waves in the presence of a quickly varying electron PSD gradient (Mann et al., 2016, 2018; Mann & Ozeke, 2016). Nevertheless, we examined Van Allen Probes data to check whether intense EMIC and chorus waves were present during the several hours of electron flux dropout leading to remnant belt formation during two events, on 24 April 2013 at ∼1–5 UT and on 7 December 2016 at ∼18–22 UT, characterized by the weakest ULF wave power at $L = 3.9$–4.6. The corresponding dropouts occurred over $L \simeq 4.1$–5.1 and over $L \sim 3.8$–5.0, respectively.

During the first event of 24 April 2013, a very weak 2-hr averaged ULF wave power ∼5 nT^2 was recorded at $L \sim 3.9$ at the Dombas station in Norway, but relatively high ULF wave power ≃70 nT^2 was still present at $L \sim 4.5$–4.6. The ULF waves at $L \sim 4.5$–4.6 are sufficiently intense to explain the electron flux dropout observed over $L \simeq 4.4$–5.0 between ∼1 UT and 5 UT on that day. Furthermore, examining data from two additional magnetometer stations located at Pinawa and Lucky Lake in central Canada shows the presence at $L \simeq 4$–4.2 of a peak of 2-hr averaged ULF wave power reaching 130 nT^2 between ∼0 UT and 2 UT on 24 April (mainly in the 18–20 MLT sector). The presence of such a high ULF wave power implies that the dropout down to $L \simeq 4.1$ recorded in the early hours of 24 April 2013 may have been produced by ULF wave-driven outward radial diffusion alone. On the same day, Mitani et al. (2018) have also found an increase of oxygen ion density and a decrease of proton density at $L = 4.4$–5 during the same 0–4 UT period (see their Figures 2 and 3). This inward propagation of oxygen ions down to $L \simeq 4.4$ is likely due to radial diffusion of ions by Pc3-Pc5 ULF waves (Mitani et al., 2018)—the same ULF waves that provided outward radial diffusion of MeV electrons. The outward PSD gradient was then negative at $L^* \geq 4.1$ for $\mu \sim$ 2,500–4,000 MeV/G electrons, favoring outward diffusion.

Intense helium-band EMIC waves (reaching ∼1 nT^2 over 10 min) and lower-band chorus waves (∼30 pT^2) were simultaneously observed by the Van Allen Probes in the 21–22 MLT and 2 MLT sectors on the same day, but only at $L \geq 4.3$ (see Figure S1). Assuming that the plasma was composed of approximately 75% protons, 20% helium ions, and 5% oxygen ions during the main phase of the storm (Ni et al., 2015; Summers, 2003), considering the cold plasma approximation for the wave dispersion relation, an electron plasma to gyrofrequency ratio $f_{pe}/f_{ce} \simeq 23$ inferred from Van Allen Probes spacecraft potential measurements (Wygant et al., 2013) during the burst of EMIC waves in the duskside plume, and with a measured upper frequency cutoff of EMIC wave power at ∼0.7 times the helium gyrofrequency, cyclotron resonance with these EMIC waves could be reached at electron energies ∼2–5 MeV (Summers, 2003). Pitch angle scattering of low equatorial pitch angle electrons by EMIC waves combined with diffusion of higher equatorial pitch angle electrons by chorus waves could therefore have contributed to the observed dropout of ultrarelativistic electrons at $L = 4.3$–4.5 (Li et al., 2007; Mourenas et al., 2016; Zhang et al., 2017). However, the contribution of EMIC and chorus waves to this dropout cannot be easily distinguished from the simultaneous contribution of fast outward radial diffusion by intense ULF waves (Mann et al., 2018), except for the fact that electron precipitation by contemporaneous EMIC and chorus waves was only operating at $L = 4.3$–4.5 whereas the dropout occurred over the whole $L = 4.1$–5.0 region located below the minimum last closed drift shell at $L = \min[L_{\mathrm{LCDS}}] \sim 5.15$.

During the second event of 7 December 2016, the maximum 2-hr averaged ULF wave power recorded at Dombas and Prince George and at Meanook and Trapper Creek stations remained low (<37 nT^2) over the whole domain $L \simeq 3.9$–4.6 during the dropout observed at $L \simeq 3.8$–4.8 between ∼17 and 24 UT. We further checked that Pinawa and Lucky Lake magnetometers at $L \simeq 4$ recorded a slightly weaker ULF wave power during the same period and that the Athabasca magnetometer from the Canadian Space Agency Geospace Observatory recorded an only slightly stronger ULF wave power at $L \sim 4.6$ than the Meanook-Trapper Creek pair of stations. Thus, ULF wave power remained consistently moderate during this event.

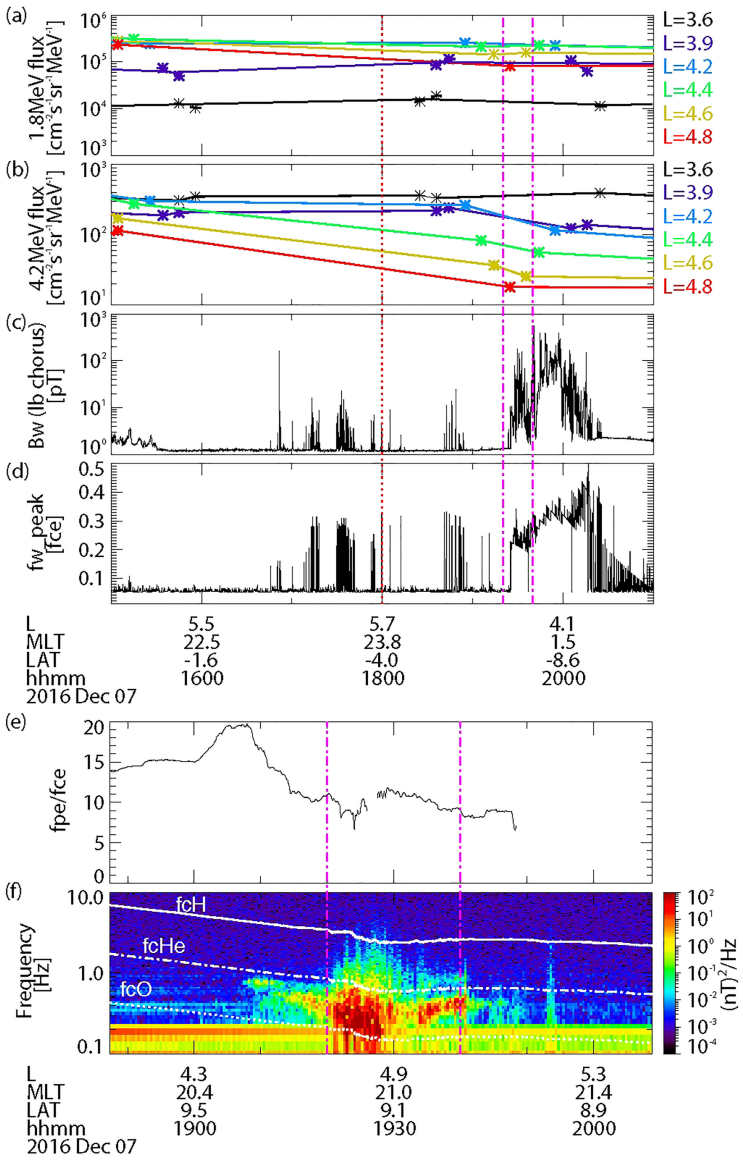

Figure 6. (a, b) Variations of omnidirectional 1.8 and 4.2 MeV electron fluxes measured by REPT on board the two Van Allen Probes as a function of time on 7 December 2016, for L = 3.6-4.8 (crosses show actual measurements). (c, d) Lower-band chorus wave root-mean-square amplitude (in pT) and peak power frequency normalized to the electron gyrofrequency, measured by Van Allen Probe A during the same period. (e, f) Helium-band and Hydrogen-band EMIC wave power as a function of time and frequency, recorded during the same period by Van Allen Probe B, and corresponding local electron plasma frequency to gyrofrequency ratio f_{pe}/f_{ce} estimated from simultaneous spacecraft potential measurements (Wygant et al., 2013). Solid, dashed-dotted, and dotted white curves indicate hydrogen, helium, and oxygen ion gyrofrequencies. A vertical red dotted line indicates 18 UT, the approximate time of minimum last closed drift shell. Vertical dashed-dotted purple lines mark the 19:20–19:40 UT interval of most intense measured EMIC waves.

Figures 6a and 6b show that both 1.8 and 4.2 MeV electron fluxes measured by the Van Allen Probes decreased significantly between 16 UT and 19 UT at $L \simeq 4.2$–4.8, whereas electron fluxes at $L = 3.6$ simultaneously remained stable from 16 UT to 20:30 UT. Electron fluxes at 0.75–1.5 MeV measured by the MagEIS instruments on the Van Allen Probes (Blake et al., 2013) varied similarly as 1.8 MeV electron fluxes measured by REPT. Such results are consistent with a dropout of >0.7 MeV electron fluxes over $L \simeq 4.2$–4.8 caused by the intense ULF waves recorded by ground magnetometers at $L \simeq 4.0$–4.6, which led to a fast outward radial diffusion toward the nearby region of depleted electron fluxes above the last closed drift shell at $L = \min[L_{\mathrm{LCDS}}] \sim 5.3$ (attained around 18 UT).

However, it is worth noting in Figures 6a and 6b the different behavior of electron fluxes between ~19 UT and 19:40–20:00 UT. During this period, the flux of 4.2 MeV electrons suddenly decreased faster than before at $L \simeq 4.2$–4.6, contrary to the flux of 1.8 MeV electrons that remained stable over $L = 3.6$–4.8 (like 0.75-1.5 MeV electron fluxes). Such a fast and energy-dependent dropout of electron flux, affecting only electrons above a minimum energy of ~2–3 MeV in less than 1 hr, is suggestive of an effect of EMIC waves. This particular period indeed contains the 19:20–19:40 UT interval during which bursts of intense EMIC and chorus waves were simultaneously recorded by the Van Allen Probes at $L \simeq 4.5$–5.0.

Figure 6c shows that Van Allen Probe A detected at 19:20–19:40 UT intense lower-band chorus waves with root-mean-square amplitudes ~70–100 pT at $L = 4.0$–5.0 in the dawn sector, while Figure 6e shows that Van Allen Probe B simultaneously recorded in the dusk sector intense (~10 nT^2) EMIC waves in the helium band, with an upper frequency cutoff generally found at ≃0.8 times the helium gyrofrequency, and intense (≈0.2 nT^2) hydrogen-band EMIC waves over a frequency range ≃0.28–0.4 times the proton gyrofrequency f_{cp}. Based on wave-normal angle measurements, such waves are mainly quasi-parallel. Assuming that such powerful EMIC waves lasted in total roughly 1 hr (UT) and were present over ~1 hr in MLT as in statistical nightside observations (Blum et al., 2017) yields hourly-averaged and MLT-averaged EMIC wave powers of ≈0.5 nT^2 in the helium band at $f/f_{cp} = 0.09$–0.2 and ≈0.01 nT^2 in the hydrogen band at $f/f_{cp} = 0.28$–0.4 over $L \sim 4.5$–5.0. However, accurately estimating the impact of EMIC waves on ultrarelativistic electrons first requires to characterize the plasma ion composition (Kersten et al., 2014; Summers, 2003).

The plasma ion composition, dominated by thermal ions with energies of about 1 eV, sets limits on EMIC wave frequencies (Kersten et al., 2014). Previous studies have estimated a helium fraction at $L = 4.3$–4.8 of the order of ≈2–5% in general in the dusk sector during moderately disturbed periods with $AE < 200$ nT, the rest of the ions being protons, except during strong geomagnetic storms where the oxygen ion fraction may reach up to 5–10% (Kersten et al., 2014; Summers, 2003; Yue et al., 2018). In the present case, as suggested by Kersten et al. (2014), we can estimate the helium ion fraction $\eta_{\mathrm{He+}}$ from the observed hydrogen-band EMIC waves. Assuming a hydrogen-helium plasma (since $D_{\mathrm{st}} > -12$ nT and $\langle AE \rangle \simeq 200$ nT during this period) and EMIC waves mainly generated with left-hand polarization near the equator as theory predicts, the so-called crossover frequency may be estimated as $f_{cr} = (1 + 15\eta_{\mathrm{He+}})^{1/2} f_{cp}/4$, with a deep minimum in EMIC wave power expected just below f_{cr} (Kersten et al., 2014). A deep minimum of wave power is seen below ≃0.28 f_{cp} at 19:20–19:40 UT in Van Allen Probe B measurements, yielding an estimate $\eta_{\mathrm{He+}} \simeq 2\%$.

Considering $\eta_{\mathrm{He+}} \simeq 2\%$, a measured upper frequency cutoff of hydrogen-band EMIC waves at ≃0.4 f_{cp} and the electron plasma frequency to gyrofrequency ratio $f_{pe}/f_{ce} \simeq 10 - 11$ inferred from Van Allen Probes spacecraft potential measurements (Wygant et al., 2013) at 19:10–19:40 UT in the dusk sector where EMIC waves are observed (see Figure 6), only electrons of energy higher than ≃2.4–2.9 MeV can reach cyclotron resonance with such waves (Summers, 2003). Considering a twice higher fraction of helium ions $\eta_{\mathrm{He+}} \sim 4\%$ merely increases the minimum electron energy by 10%. As regards helium-band EMIC wave with an upper frequency cutoff at ≃0.2 f_{cp} in general over 19:10–19:40 UT, cyclotron resonance with these waves requires electron energies above ≃5–6 MeV for $\eta_{\mathrm{He+}} \sim 2\%$ and above ≃4–5 MeV for $\eta_{\mathrm{He+}} \sim 4\%$ (Summers, 2003). Note that EMIC waves were observed in a sector of high plasma density inside a plasmasphere slightly more extended on the duskside (with an estimated minimum $L_{\mathrm{pp}} \simeq 4.7$ there), while contemporaneous chorus waves recorded in the dawn sector were very probably in a lower density region with $f_{pe}/f_{ce} \sim 4$–5 just above a lower plasmapause in this MLT sector (Agapitov et al., 2019; Meredith et al., 2003). Unfortunately, no plasma density measurements are available at that time in the dawn sector.

Based on analytical estimates of electron loss rates validated against simulations and observations (Mourenas et al., 2016; Zhang et al., 2017), and considering the above wave and plasma parameters, the measured duskside hydrogen-band EMIC waves together with the contemporaneous dawnside chorus waves could have precipitated approximately half of the ~3-5 MeV electrons at $L \simeq 4.5$–5 between 19 UT and 20 UT without affecting lower energy electrons, in rough agreement with observations in Figures 6a and 6b. The measured helium-band EMIC waves together with the same chorus waves could have produced a similar electron precipitation over a slightly higher energy range ~4–6 MeV (Kersten et al., 2014; Ni et al., 2015; Summers, 2003). Although some EMIC wave power sometimes nearly reaches the helium gyrofrequency in Figure 6f, hot plasma effects (neglected in the above estimates) are then expected to keep the minimum energy of electrons precipitated by such waves above at least ~1–2 MeV (Chen et al., 2013). This is confirmed

by the stronger PSD drop observed at $L^* \sim 4.5$–5 for $\mu > 2{,}500$ MeV/G. EMIC waves likely increased electron loss in this domain as compared with ULF wave-driven outward diffusion loss, which also occurred at lower energy.

Therefore, the above investigation provides evidence that contemporaneous EMIC and chorus waves likely played an important role in the creation of an URRB on 7 December 2016, by contributing to the 19–20 UT dropout of multi-MeV electrons, together with fast outward radial diffusion by the simultaneously measured intense ULF waves.

4. Conclusions

In the present paper, we explored the probable causes of the high-L dropout of electron flux that leads to the formation of URRBs at $L \sim 3$–3.5 for 18 different events previously reported by Pinto et al. (2018). Based on 2012–2017 observations from the Van Allen Probes and ground magnetometer measurements of Pc3-Pc5 ULF waves, we have shown that the upper edge of these remnant belts is correlated with both the minimum plasmapause position and the minimum last closed drift shell of trapped electrons. We further found that the maximum 2-hr radial diffusion rate between the upper edge of the remnant belts and the last closed drift shell, estimated based on ULF wave power recorded at $L \sim 3.9$ during each dropout, is also correlated with the minimum last closed drift shell and the upper extent of the remnant belts. ULF waves often reach a high integrated power at low L shells down to the minimum plasmapause location. The corresponding ULF wave-driven radial diffusion is therefore more likely to reach a high intensity at lower L shells when the plasmapause and the last closed drift shell come closer to the Earth—potentially allowing to confine URRBs to lower L shells in less than 2–4 hr. In addition, the PSD of multi-MeV electrons generally exhibits the needed negative or oscillating outward radial gradient between the minimum location of 4 MeV electron flux drop and the minimum last closed drift shell. Therefore, electron outward radial diffusion by intense ULF waves is a very good candidate, together with magnetopause shadowing, to explain the electron losses between the last closed drift shells and the plasmapause location for the studied URRBs events and, thus, important for the location and formation of remnant belts.

An analysis of two remnant belts characterized by a weaker ULF wave power during the dropout interval has shown that additional multi-MeV electron precipitation through combined scattering by contemporaneous EMIC and lower-band chorus waves is probably contributing in at least a finite number of events. A more comprehensive MLT and L-shell coverage by multiple satellites at a higher temporal resolution would be needed to assess more precisely the relative importance of these different processes in the formation of URRBs.

Acknowledgments
V. A. P. thanks the support of Becas Chile program. J. B. would like to acknowledge NASA Awards NNX16AG21G and NNX14AN85G and AFOSR Award FA9550-15-1-0158. P. S. M. is grateful for the support of CONICYT Chile FONDECYT Grant 1191351. The work of X.-J. Z. was supported by RBSP-EMFISIS and RBSP-ECT funding 443956-TH-81074 and 443956-TH-79425 under NASA's Prime Contract NNN06AA01C. We gratefully acknowledge Van Allen Probes ECT-REPT/MagEIS and EMFISIS data (obtained from https://www.rbsp-ect.lanl.gov/ and https://emfisis.physics.uiowa.edu/data/). We are also grateful to S. Mende and C. T. Russell for the Prince George and Athabasca magnetometer data from the THEMIS GMAG network (available at http://themis.igpp.ucla.edu/gmag&urluscore;desc.shtml) (where magnetometer data from the following stations are also available), the AUTUMNX magnetometer network funded through the Canadian Space Agency Geospace Observatory for the Athabasca University magnetometer data (at http://autumn.athabascau.ca/), the Tromso Geophysical Observatory, University of Tromso Norway, for the Dombas magnetometer data (at http://flux.phys.uit.no/geomag.html), the Geophysical Institute of the University of Alaska (at http://magnet.asf.alaska.edu/) for the Trapper Creek magnetometer data, and the Canadian Magnetic Observatory Network maintained and operated by the Geological Survey of Canada (at https://www.geomag.nrcan.gc.ca/index-en.php) for the Meanook magnerometer data used in this study. We also thank I. R. Mann, D. K. Milling, and the CARISMA team for the PINA and LCL magnetometer data (obtained from http://data.carisma.ca), provided by the University of Alberta with funding from the Canadian Space Agency. We thank J. Goldstein for plasmasphere simulations (available at http://enarc.space.swri.edu/PTP/) and the Los Alamos National Laboratory for the LANL* code (available at https://pythonhosted.org/SpacePy/) We also acknowledge the CXD team at LANL for GPS electron flux measurements (available from NOAA at https://www.ngdc.noaa.gov/stp/spaceweather/satellite-data/satellitesystems/gps/). OMNI data were obtained from CDAWeb (https://cdaweb.gsfc.nasa.gov). All the supporting information used in this manuscript are publicly available in the Figshare data repository (at https://doi.org/10.6084/m9.figshare.11871174.v1).

References

Agapitov, O., Mourenas, D., Artemyev, A., Hospodarsky, G., & Bonnell, J. W. (2019). Time scales for electron quasi-linear diffusion by lower-band chorus waves: The effects of ω_{pe} / Ω_{ce} dependence on geomagnetic activity. *Geophysical Research Letters*, *46*, 6178–6187. https://doi.org/10.1029/2019GL083446

Albert, J. M., Selesnick, R. S., Morley, S. K., Henderson, M. G., & Kellerman, A. C. (2018). Calculation of last closed drift shells for the 2013 GEM radiation belt challenge events. *Journal of Geophysical Research: Space Physics*, *123*, 9597–9611. https://doi.org/10.1029/2018JA025991

Baker, D. N., Kanekal, S. G., Hoxie, V. C., Batiste, S., Bolton, M., Li, X., et al. (2013). The Relativistic Electron-Proton Telescope (REPT) instrument on board the Radiation Belt Storm Probes (RBSP) spacecraft: Characterization of Earth's radiation belt high-energy particle populations. *Space Science Reviews*, *179*(1-4), 337–381. https://doi.org/10.1007/s11214-012-9950-9

Baker, D. N., Kanekal, S. G., Hoxie, V. C., Henderson, M. G., Li, X., Spence, H. E., et al. (2013). A long-lived relativistic electron storage ring embedded in Earth's outer Van Allen belt. *Science*, *340*(6129), 186–190. https://doi.org/10.1126/science.1233518

Blake, J. B., Carranza, P. A., Claudepierre, S. G., Clemmons, J. H., Crain, W. R., Dotan, Y., et al. (2013). The Magnetic Electron Ion Spectrometer (MagEIS) instruments aboard the Radiation Belt Storm Probes (RBSP) spacecraft. *Space Science Reviews*, *179*(1-4), 383–421. https://doi.org/10.1007/s11214-013-9991-8

Blum, L. W., Bonnell, J. W., Agapitov, O., Paulson, K., & Kletzing, C. (2017). EMIC wave scale size in the inner magnetosphere: Observations from the dual Van Allen Probes. *Geophysical Research Letters*, *44*, 1227–1233. https://doi.org/10.1002/2016GL072316

Boynton, R. J., Mourenas, D., & Balikhin, M. A. (2017). Electron flux dropouts at $L \sim 4.2$ from Global Positioning System satellites: Occurrences, magnitudes, and main driving factors. *Journal of Geophysical Research: Space Physics*, *122*, 11,428–11,441. https://doi.org/10.1002/2017JA024523

Chen, L., Thorne, R. M., Shprits, Y., & Ni, B. (2013). An improved dispersion relation for parallel propagating electromagnetic waves in warm plasmas: Application to electron scattering. *Journal of Geophysical Research: Space Physics*, *118*, 2185–2195. https://doi.org/10.1002/jgra.50260

Claudepierre, S. G., O'Brien, T. P., Blake, J. B., Fennell, J. F., Roeder, J. L., Clemmons, J. H., et al. (2015). A background correction algorithm for Van Allen Probes MagEIS electron flux measurements. *Journal of Geophysical Research: Space Physics*, *120*, 5703–5727. https://doi.org/10.1002/2015JA021171

Degeling, A. W., Rae, I. J., Watt, C. E. J., Shi, Q. Q., Rankin, R., & Zong, Q.-G. (2018). Control of ULF wave accessibility to the inner magnetosphere by the convection of plasma density. *Journal of Geophysical Research: Space Physics*, *123*, 1086–1099. https://doi.org/10.1002/2017JA024874

Ganushkina, N. Y., Amariutei, O. A., Shprits, Y. Y., & Liemohn, M. W. (2013). Transport of the plasma sheet electrons to the geostationary distances. *Journal of Geophysical Research: Space Physics*, *118*, 82–98. https://doi.org/10.1029/2012JA017923

Goldstein, J., Thomsen, M. F., & DeJong, A. (2014). In situ signatures of residual plasmaspheric plumes: Observations and simulation. *Journal of Geophysical Research: Space Physics*, *119*, 4706–4722. https://doi.org/10.1002/2014JA019953

Green, J. C. (2004). Relativistic electrons in the outer radiation belt: Differentiating between acceleration mechanisms. *Journal of Geophysical Research*, *109*, A03213. https://doi.org/10.1029/2003JA010153

Hao, Y. X., Zong, Q.-G., Zhou, X.-Z., Rankin, R., Chen, X. R., Liu, Y., et al. (2019). Global-scale ULF waves associated with SSC accelerate magnetospheric ultrarelativistic electrons. *Journal of Geophysical Research: Space Physics*, *124*, 1525–1538. https://doi.org/10.1029/2018JA026134

Hao, Y. X., Zong, Q.-G., Zhou, X.-Z., Rankin, R., Chen, X. R., Liu, Y., et al. (2017). Relativistic electron dynamics produced by azimuthally localized poloidal mode ULF waves: Boomerang-shaped pitch angle evolutions. *Geophysical Research Letters*, *44*, 7618–7627. https://doi.org/10.1002/2017GL074006

Hartinger, M., Moldwin, M. B., Angelopoulos, V., Takahashi, K., Singer, H. J., Anderson, R. R., et al. (2010). Pc5 wave power in the quiet-time plasmasphere and trough. *Geophysical Research Letters*, *37*, L07107. https://doi.org/10.1029/2010GL042475

Kersten, T., Horne, R. B., Glauert, S. A., Meredith, N. P., Fraser, B. J., & Grew, R. S. (2014). Electron losses from the radiation belts caused by EMIC waves. *Journal of Geophysical Research: Space Physics*, *119*, 8820–8837. https://doi.org/10.1002/2014JA020366

Kim, H.-J., & Chan, A. A. (1997). Fully adiabatic changes in storm time relativistic electron fluxes. *Journal of Geophysical Research*, *102*(A10), 22,107–22,116. https://doi.org/10.1029/97JA01814

Kletzing, C. A., Kurth, W. S., Acuna, M., MacDowall, R. J., Torbert, R. B., Averkamp, T., et al. (2013). The Electric and Magnetic Field Instrument Suite and Integrated Science (EMFISIS) on RBSP. *Space Science Reviews*, *179*(1-4), 127–181. https://doi.org/10.1007/s11214-013-9993-6

Kubota, Y., & Omura, Y. (2018). Nonlinear dynamics of radiation belt electrons interacting with chorus emissions localized in longitude. *Journal of Geophysical Research: Space Physics*, *123*, 4835–4857. https://doi.org/10.1029/2017JA025050

Kurth, W. S., De Pascuale, S., Faden, J. B., Kletzing, C. A., Hospodarsky, G. B., Thaller, S., & Wygant, J. R. (2015). Electron densities inferred from plasma wave spectra obtained by the waves instrument on Van Allen Probes: Van Allen Probes electron densities. *Journal of Geophysical Research: Space Physics*, *120*, 904–914. https://doi.org/10.1002/2014JA020857

Li, W., Ma, Q., Thorne, R. M., Bortnik, J., Kletzing, C. A., Kurth, W. S., et al. (2015). Statistical properties of plasmaspheric hiss derived from Van Allen Probes data and their effects on radiation belt electron dynamics. *Journal of Geophysical Research: Space Physics*, *120*, 3393–3405. https://doi.org/10.1002/2015JA021048

Li, W., Shprits, Y. Y., & Thorne, R. M. (2007). Dynamic evolution of energetic outer zone electrons due to wave-particle interactions during storms. *Journal of Geophysical Research*, *112*, A10220. https://doi.org/10.1029/2007JA012368

Li, W., Thorne, R. M., Ma, Q., Ni, B., Bortnik, J., Baker, D. N., et al. (2014). Radiation belt electron acceleration by chorus waves during the 17 March 2013 storm. *Journal of Geophysical Research: Space Physics*, *119*, 4681–4693. https://doi.org/10.1002/2014JA019945

Li, L., Zhou, X.-Z., Zong, Q.-G., Rankin, R., Zou, H., Liu, Y., et al. (2017). Charged particle behavior in localized ultralow frequency waves: Theory and observations. *Geophysical Research Letters*, *44*, 5900–5908. https://doi.org/10.1002/2017GL073392

Loridan, V., Ripoll, J.-F., Tu, W., & Scott Cunningham, Gregory (2019). On the use of different magnetic field models for simulating the dynamics of the outer radiation belt electrons during the October 1990 storm. *Journal of Geophysical Research: Space Physics*, *124*, 6453–6486. https://doi.org/10.1029/2018JA026392

Lyons, L. R., Thorne, R. M., & Kennel, C. F. (1972). Pitch-angle diffusion of radiation belt electrons within the plasmasphere. *Journal of Geophysical Research*, *77*(19), 3455–3474. https://doi.org/10.1029/JA077i019p03455

Mann, I. R., Lee, E. A., Claudepierre, S. G., Fennell, J. F., Degeling, A., Rae, I. J., et al. (2013). Discovery of the action of a geophysical synchrotron in the Earth's Van Allen radiation belts. *Nature Communications*, *4*(1), 2795. https://doi.org/10.1038/ncomms3795

Mann, I. R., Murphy, K. R., Ozeke, L. G., Rae, I. J., Milling, D. K., Kale, A. A., & Honary, F. F. (2013). The role of ultralow frequency waves in radiation belt dynamics. In D. Summers (Eds.), *Dynamics of the Earth's radiation belts and inner magnetosphere* (pp. 69–92), *Geophysical Monograph Series*. Washington, DC: American Geophysical Union. https://doi.org/10.1029/2012GM001349

Mann, I. R., & Ozeke, L. G. (2016). How quickly, how deeply, and how strongly can dynamical outer boundary conditions impact Van Allen radiation belt morphology? *Journal of Geophysical Research: Space Physics*, *121*, 5553–5558. https://doi.org/10.1002/2016JA022647

Mann, I. R., Ozeke, L. G., Morley, S. K., Murphy, K. R., Claudepierre, S. G., Turner, D. L., et al. (2018). Reply to 'The dynamics of Van Allen belts revisited'. *Nature Physics*, *14*(2), 103–104. https://doi.org/10.1038/nphys4351

Mann, I. R., Ozeke, L. G., Murphy, K. R., Claudepierre, S. G., Turner, D. L., Baker, D. N., et al. (2016). Explaining the dynamics of the ultra-relativistic third Van Allen radiation belt. *Nature Physics*, *12*(10), 978–983. https://doi.org/10.1038/nphys3799

Mauk, B. H., Fox, N. J., Kanekal, S. G., Kessel, R. L., Sibeck, D. G., & Ukhorskiy, A. (2013). Science objectives and rationale for the Radiation Belt Storm Probes mission. *Space Science Reviews*, *179*(1-4), 3–27. https://doi.org/10.1007/s11214-012-9908-y

Mende, S. B., Harris, S. E., Frey, H. U., Angelopoulos, V., Russell, C. T., Donovan, E., et al. (2008). The THEMIS array of ground-based observatories for the study of auroral substorms. *Space Science Reviews*, *141*(1-4), 357–387. https://doi.org/10.1007/s11214-008-9380-x

Meredith, N. P., Horne, R. B., Thorne, R. M., & Anderson, R. R. (2003). Favored regions for chorus-driven electron acceleration to relativistic energies in the Earth's outer radiation belt. *Geophysical Research Letters*, *30*(16), 1871. https://doi.org/10.1029/2003GL017698

Mitani, K., Seki, K., Keika, K., Gkioulidou, M., Lanzerotti, L. J., Mitchell, D. G., & Kletzing, C. A. (2018). Radial transport of higher-energy oxygen ions into the deep inner magnetosphere observed by Van Allen Probes. *Geophysical Research Letters*, *45*, 4534–4541. https://doi.org/10.1029/2018GL077500

Morley, S. K., Sullivan, J. P., Henderson, M. G., Blake, J. B., & Baker, D. N. (2016). The Global Positioning System constellation as a space weather monitor: Comparison of electron measurements with Van Allen Probes data. *Space Weather*, *14*(2), 76–92. https://doi.org/10.1002/2015SW001339

Mourenas, D., Artemyev, A. V., Ma, Q., Agapitov, O. V., & Li, W. (2016). Fast dropouts of multi-MeV electrons due to combined effects of EMIC and whistler mode waves. *Geophysical Research Letters*, *43*, 4155–4163. https://doi.org/10.1002/2016GL068921

Mourenas, D., Ma, Q., Artemyev, A. V., & Li, W. (2017). Scaling laws for the inner structure of the radiation belts. *Geophysical Research Letters*, *44*, 3009–3018. https://doi.org/10.1002/2017GL072987

Mourenas, D., Zhang, X.-J., Artemyev, A. V., Angelopoulos, V., Thorne, R. M., Bortnik, J., et al. (2018). Electron nonlinear resonant interaction with short and intense parallel chorus wave packets. *Journal of Geophysical Research: Space Physics*, *123*, 4979–4999. https://doi.org/10.1029/2018JA025417

Moya, P. S., Pinto, V. A., Sibeck, D. G., Kanekal, S. G., & Baker, D. N. (2017). On the effect of geomagnetic storms on relativistic electrons in the outer radiation belt: Van Allen Probes observations. *Journal of Geophysical Research: Space Physics*, *122*, 11,100–11,108. https://doi.org/10.1002/2017JA024735

Murphy, K. R., Mann, I. R., & Sibeck, D. G. (2015). On the dependence of storm time ULF wave power on magnetopause location: Impacts for ULF wave radial diffusion. *Geophysical Research Letters*, *42*, 9676–9684. https://doi.org/10.1002/2015GL066592

Ni, B., Cao, X., Zou, Z., Zhou, C., Gu, X., Bortnik, J., et al. (2015). Resonant scattering of outer zone relativistic electrons by multiband EMIC waves and resultant electron loss time scales. *Journal of Geophysical Research: Space Physics*, *120*, 7357–7373. https://doi.org/10.1002/2015JA021466

O'Brien, T. P., & Moldwin, M. B. (2003). Empirical plasmapause models from magnetic indices. *Geophysical Research Letters*, *30*(4), 1152. https://doi.org/10.1029/2002GL016007

Olifer, L. (2019). On the signatures of magnetopause shadowing losses in the Van Allen radiation belts of the Earth (Master's Thesis), University of Alberta Libraries. https://doi.org/10.7939/R3-5GHR-A760

Olifer, L., Mann, I. R., Morley, S. K., Ozeke, L. G., & Choi, D. (2018). On the role of last closed drift shell dynamics in driving fast losses and Van Allen radiation belt extinction. *Journal of Geophysical Research: Space Physics*, *123*, 3692–3703. https://doi.org/10.1029/2018JA025190

Ouyang, X. Y., Bortnik, J., Ren, J., & Berthelier, J. J. (2019). Features of nightside ULF wave activity in the ionosphere. *Journal of Geophysical Research: Space Physics*, *124*, 9203–9213. https://doi.org/10.1029/2019JA027103

Ozeke, L., Mann, I., Dufresne, S., Olifer, L., Morley, S., Claudepierre, S., et al. (2019). Rapid outer radiation belt flux dropouts and fast acceleration during the March 2015 and 2013 storms: Role of ULF wave transport from a dynamic outer boundary. *Earth and Space Science Open Archive*, *125*, e2019JA027179. https://doi.org/10.1002/essoar.10501063.1

Ozeke, L. G., Mann, I. R., Murphy, K. R., Degeling, A. W., Claudepierre, S. G., & Spence, H. E. (2018). Explaining the apparent impenetrable barrier to ultra-relativistic electrons in the outer Van Allen belt. *Nature Communications*, *9*(1), 1844. https://doi.org/10.1038/s41467-018-04162-3

Ozeke, L. G., Mann, I. R., Murphy, K. R., Jonathan Rae, I., & Milling, D. K. (2014). Analytic expressions for ULF wave radiation belt radial diffusion coefficients: Analytic radial diffusion coefficients. *Journal of Geophysical Research: Space Physics*, *119*, 1587–1605. https://doi.org/10.1002/2013JA019204

Pahud, D. M., Rae, I. J., Mann, I. R., Murphy, K. R., & Amalraj, V. (2009). Ground-based Pc5 ULF wave power: Solar wind speed and MLT dependence. *Journal of Atmospheric and Solar-Terrestrial Physics*, *71*(10-11), 1082–1092. https://doi.org/10.1016/j.jastp.2008.12.004

Pinto, V. A., Bortnik, J., Moya, P. S., Lyons, L. R., Sibeck, D. G., Kanekal, S. G., et al. (2018). Characteristics, occurrence, and decay rates of remnant belts associated with three-belt events in the Earth's radiation belts. *Geophysical Research Letters*, *45*, 12,099–12,107. https://doi.org/10.1029/2018GL080274

Pinto, V. A., Mourenas, D., Bortnik, J., Zhang, X.-J., Artemyev, A. V., Moya, P. S., & Lyons, L. R. (2019). Decay of ultrarelativistic remnant belt electrons through scattering by plasmaspheric hiss. *Journal of Geophysical Research: Space Physics*, *124*, 5222–5233. https://doi.org/10.1029/2019JA026509

Rae, I. J., Murphy, K. R., Watt, C. E. J., Sandhu, J. K., Georgiou, M., Degeling, A. W., et al. (2019). How do ultra-low frequency waves access the inner magnetosphere during geomagnetic storms? *Geophysical Research Letters*, *46*, 10,699–10,709. https://doi.org/10.1029/2019GL082395

Ren, J., Zong, Q.-G., Miyoshi, Y., Zhou, X. Z., Wang, Y. F., Rankin, R., et al. (2017). Low-energy (<200 eV) electron acceleration by ULF waves in the plasmaspheric boundary layer: Van Allen Probes observation. *Journal of Geophysical Research: Space Physics*, *122*, 9969–9982. https://doi.org/10.1002/2017JA024316

Schulz, M. (1991). The magnetosphere, *Geomagnetism* (pp. 87–293): Elsevier. https://doi.org/10.1016/B978-0-12-378674-6.50008-X

Schulz, M., & Lanzerotti, L. J. (1974). *Particle diffusion in the radiation belts*, Physics and Chemistry in Space, (vol. 7). Berlin, Heidelberg: Springer Berlin Heidelberg. https://doi.org/10.1007/978-3-642-65675-0

Shprits, Y. Y., Horne, R. B., Kellerman, A. C., & Drozdov, A. Y. (2018). The dynamics of Van Allen belts revisited. *Nature Physics*, *14*(2), 102–103. https://doi.org/10.1038/nphys4350

Shprits, Y. Y., Subbotin, D., Drozdov, A., Usanova, M. E., Kellerman, A., Orlova, K., et al. (2013). Unusual stable trapping of the ultrarelativistic electrons in the Van Allen radiation belts. *Nature Physics*, *9*(11), 699–703. https://doi.org/10.1038/nphys2760

Spence, H. E., Reeves, G. D., Baker, D. N., Blake, J. B., Bolton, M., Bourdarie, S., et al. (2013). Science goals and overview of the Radiation Belt Storm Probes (RBSP) Energetic Particle, Composition, and Thermal Plasma (ECT) suite on NASA's Van Allen Probes mission. *Space Science Reviews*, *179*(1-4), 311–336. https://doi.org/10.1007/s11214-013-0007-5

Summers, D. (2003). Relativistic electron pitch-angle scattering by electromagnetic ion cyclotron waves during geomagnetic storms. *Journal of Geophysical Research*, *108*(A4), 1143. https://doi.org/10.1029/2002JA009489

Thorne, R. M., Li, W., Ni, B., Ma, Q., Bortnik, J., Baker, D. N., et al. (2013). Evolution and slow decay of an unusual narrow ring of relativistic electrons near L ∼ 3.2 following the September 2012 magnetic storm. *Geophysical Research Letters*, *40*, 3507–3511. https://doi.org/10.1002/grl.50627

Tsyganenko, N. A. (1995). Modeling the Earth's magnetospheric magnetic field confined within a realistic magnetopause. *Journal of Geophysical Research*, *100*(A4), 5599. https://doi.org/10.1029/94JA03193

Tsyganenko, N. A. (2005). Modeling the dynamics of the inner magnetosphere during strong geomagnetic storms. *Journal of Geophysical Research*, *110*, A03208. https://doi.org/10.1029/2004JA010798

Turner, D. L., Angelopoulos, V., Li, W., Hartinger, M. D., Usanova, M., Mann, I. R., et al. (2013). On the storm-time evolution of relativistic electron phase space density in Earth's outer radiation belt. *Journal of Geophysical Research: Space Physics*, *118*, 2196–2212. https://doi.org/10.1002/jgra.50151

Turner, D. L., Angelopoulos, V., Shprits, Y., Kellerman, A., Cruce, P., & Larson, D. (2012). Radial distributions of equatorial phase space density for outer radiation belt electrons. *Geophysical Research Letters*, *39*, L09101. https://doi.org/10.1029/2012GL051722

Turner, D. L., & Ukhorskiy, A. Y. (2020). Outer radiation belt losses by magnetopause incursions and outward radial transport: New insight and outstanding questions from the Van Allen Probes era, *The dynamic loss of Earth's radiation belts* (pp. 1–28): Elsevier. https://doi.org/10.1016/B978-0-12-813371-2.00001-9

Wang, C., Zong, Q., & Wang, Y. (2010). Propagation of interplanetary shock excited ultra low frequency (ULF) waves in magnetosphere-ionosphere-atmosphere—Multi-spacecraft "Cluster" and ground-based magnetometer observations. *Science China Technological Sciences*, *53*(9), 2528–2534. https://doi.org/10.1007/s11431-010-4064-7

Wygant, J. R., Bonnell, J. W., Goetz, K., Ergun, R. E., Mozer, F. S., Bale, S. D., et al. (2013). The electric field and waves instruments on the Radiation Belt Storm Probes mission. *Space Science Reviews*, *179*(1-4), 183–220. https://doi.org/10.1007/s11214-013-0013-7

Xiang, Z., Tu, W., Ni, B., Henderson, M. G., & Cao, X. (2018). A statistical survey of radiation belt dropouts observed by Van Allen Probes. *Geophysical Research Letters*, *45*, 8035–8043. https://doi.org/10.1029/2018GL078907

Yu, Y., Koller, J., Zaharia, S., & Jordanova, V. (2012). *L** neural networks from different magnetic field models and their applicability. *Space Weather*, *10*, S02014. https://doi.org/10.1029/2011SW000743

Yuan, C., & Zong, Q. (2013). The double-belt outer radiation belt during CME- and CIR-driven geomagnetic storms. *Journal of Geophysical Research: Space Physics*, *118*, 6291–6301. https://doi.org/10.1002/jgra.50564

Yue, C., Bortnik, J., Li, W., Ma, Q., Gkioulidou, M., Reeves, G. D., et al. (2018). The composition of plasma inside geostationary orbit based on Van Allen Probes observations. *Journal of Geophysical Research: Space Physics*, *123*, 6478–6493. https://doi.org/10.1029/2018JA025344

Zhang, X.-J., Li, W., Thorne, R. M., Angelopoulos, V., Bortnik, J., Kletzing, C. A., et al. (2016). Statistical distribution of EMIC wave spectra: Observations from Van Allen Probes. *Geophysical Research Letters*, *43*, 12,348–12,355. https://doi.org/10.1002/2016GL071158

Zhang, X.-J., Mourenas, D., Artemyev, A. V., Angelopoulos, V., & Thorne, R. M. (2017). Contemporaneous EMIC and whistler mode waves: Observations and consequences for MeV electron loss. *Geophysical Research Letters*, *44*, 8113–8121. https://doi.org/10.1002/2017GL073886

Zong, Q., Rankin, R., & Zhou, X. (2017). The interaction of ultra-low-frequency pc3-5 waves with charged particles in Earth's magnetosphere. *Reviews of Modern Plasma Physics*, *1*(1), 10. https://doi.org/10.1007/s41614-017-0011-4

Zong, Q.-G., Zhou, X.-Z., Wang, Y. F., Li, X., Song, P., Baker, D. N., et al. (2009). Energetic electron response to ULF waves induced by interplanetary shocks in the outer radiation belt. *Journal of Geophysical Research*, *114*, A10204. https://doi.org/10.1029/2009JA014393